

Elastic Shape Analysis of Movement Data

J.E. Borgert¹, Jan Hannig¹, J.D. Tucker², Liubov Arbeeva³, Ashley N. Buck^{3,4,5},
Yvonne M. Golightly^{3,6,7}, Stephen P. Messier⁸,
Amanda E. Nelson^{3,7,9}, J.S. Marron¹

¹Department of Statistics & Operations Research, University of North Carolina, Chapel Hill, NC

²Statistical Sciences, Sandia National Laboratories, Albuquerque, NM

³Thurston Arthritis Research Center, University of North Carolina, Chapel Hill, NC

⁴Human Movement Science Curriculum, University of North Carolina, Chapel Hill, NC

⁵Department of Exercise & Sport Science, University of North Carolina, Chapel Hill, NC

⁶College of Allied Health Professions, University of Nebraska Medical Center, Omaha, NE

⁷Department of Epidemiology, Gillings School of Global Public Health, University of North Carolina, Chapel Hill, NC

⁸Department of Health & Exercise Science, Wake Forest University, Winston-Salem, NC

⁹Department of Medicine, University of North Carolina, Chapel Hill, NC

Abstract

Osteoarthritis (OA) is a prevalent degenerative joint disease, with the knee being the most commonly affected joint. Modern studies of knee joint injury and OA often measure biomechanical variables, particularly forces exerted during walking. However, the relationship among gait patterns, clinical profiles, and OA disease remains poorly understood. These biomechanical forces are typically represented as curves over time, but until recently, studies have relied on discrete values (or *landmarks*) to summarize these curves. This work aims to demonstrate the added value of analyzing full movement curves over conventional discrete summaries. Using data from the Intensive Diet and Exercise for Arthritis (IDEA) study (Messier et al., 2009, 2013), we developed a shape-based representation of variation in the full biomechanical curves. Compared to conventional discrete summaries, our approach yields more powerful predictors of disease progression and relevant clinical traits, as demonstrated by a nested model comparison. Notably, our work is among the first to use movement curves to predict disease progression and to quantitatively evaluate the added value of analyzing full movement curves over conventional discrete summaries.

Keywords: Functional data analysis, Ground reaction forces, Human movement data, Object oriented data analysis, Osteoarthritis, Shape statistics

1 Introduction

Osteoarthritis (OA) is a prevalent degenerative joint disease characterized by cartilage loss, bone and soft tissue changes, joint pain, and diminished function. In the United States, OA affects at least 19% of adults aged 45 years and older, with the knee being the most frequently affected joint, accounting for more than 80% of the total burden of the disease (Dillon et al., 2006; Jordan et al., 2007; Lawrence et al., 2008; Vos et al., 2012). Knee OA is characterized by both the severity of radiographic damage and clinical symptoms, such as in knee pain and function. Previous research, such as in (Zhang and Jordan, 2010), indicated that risk factors and disease progression may vary by clinical phenotype. Additionally, important work like Felson (2013) and Guilak (2011) identified biomechanical factors in the etiology and pathogenesis of knee OA.

Biomechanical variables, particularly forces exerted during walking, are often measured in modern studies of joint injury and OA. However, the relationship among gait patterns, clinical profiles, and OA disease remains poorly understood. Biomechanical forces, collected continuously during gait analysis, are typically represented as curves over time. Discrete summaries, such as peak values, are commonly used to analyze patterns in *joint loading* (forces acting on the knee joint). Such discrete summaries are called *landmarks* in the shape statistics terminology of Dryden and Mardia (2016). Analyses based on conventional discrete summaries, such as those by Sims et al. (2009) and Astephen et al. (2008), have identified differences between groups (e.g., sex differences) and indicated variations in gait patterns which contribute to knee OA-related outcomes. Recent work by Buck et al. (2024) evaluated the ability of various clinical traits and conventional discrete summaries of gait forces to predict early symptomatic knee OA. While simplifying the statistical methods required for analysis, relying on conventional discrete summaries risks overlooking

information encoded in the complete range and patterns of movement data. Research by [Muniz et al. \(2006\)](#), [Costello et al. \(2021\)](#), [Bjornsen et al. \(2024\)](#), [Davis et al. \(2019\)](#), and others has demonstrated the value of analyzing full movement curves. However, these studies are limited and have not been formally compared to analyses based on conventional discrete summaries. For harmonic analyses of full movement curves, see [Trentadue and Schmitt \(2024\)](#) and references therein.

The primary goal of this work is to demonstrate the value added from analyzing full movement curves over conventional discrete summaries. We take an Object Oriented Data Analysis (OODA) approach for this analysis. OODA, described in [Marron and Dryden \(2021\)](#), is a framework for interdisciplinary research that introduces new terminology and methodologies for analyzing complex data. It emphasizes the careful selection of relevant data objects and the utilization of methods intrinsic to the corresponding object spaces. This approach enables the consideration of full movement data curves as complex data objects in high-dimensional space. Furthermore, the richer information within these curves presents numerous choices for both the *data object* of interest and the appropriate methodology for analysis.

Using data from the Intensive Diet and Exercise for Arthritis (IDEA) study ([Messier et al., 2009, 2013](#)), we developed a shape-based representation of variation in the full biomechanical curves. Our approach, compared to conventional discrete summaries, yields more powerful predictors of disease progression and relevant clinical traits, as demonstrated by a nested model comparison. Notably, our work is among the first to use movement curves to predict disease progression and to quantitatively evaluate the added value of utilizing full movement curves as predictors over conventional discrete summaries.

2 Curves as data objects

For the IDEA study, participants wore laboratory-provided cushioned shoes and walked at their preferred speed on a 22.5m walkway. Kinetic data, including Ground Reaction Force (GRF), were collected using an Advanced Medical Technologies, Inc. model OR-6-5-1 force plate (480 Hz) and filtered using a 4th order low-pass Butterworth filter with a cutoff frequency of 6 Hz. The GRF consists of three components: vertical GRF (vGRF), representing the force exerted downwards; anterior-posterior GRF (apGRF), the propulsive or braking force in the direction of walking; and medial-lateral GRF (mlGRF) in the third orthogonal direction.

When plotted as a function of time, the horizontal axis reflects the percentage of *stance* (time interval of foot contact with the ground) over a gait cycle with body weight-normalized force values (measured in Newtons) on the vertical axis.

Successful walking trials required the entire foot to be on the force plate during the stance phase, with participants maintaining their preferred speed within $\pm 3.5\%$.

We studied the part of the IDEA data that contained measurements of each GRF component taken at a constant sampling rate over the duration of each step. For each IDEA participant, three trials per limb were collected. For some participants, one or more trials were missing from the data. In those cases, we used as many trials as were given in the data and did not impute. We considered the collection of all trials of both limbs of all participants.

The complete set of curves for each GRF component contained 2686 curves from 454 participants. The top left panel of Figure 1 shows the collection of raw data vGRF curves colored by walking speed. There, the rainbow descends from fastest walking speed (red) to slowest (purple). Notice that many of those curves have consecutive starting and trailing

zeros, which are outside the stance phase (i.e., after the foot has left contact with the force plate, but force data were still being collected) and hence do not correspond to a meaningful part of the measurements. Consequently, we define the beginning of the force curve as the zero value immediately preceding the first nonzero value, and similarly, the end of the curve as the zero value immediately following the last non-zero value. To establish a common time axis across all curves, we utilized the relevant segment of each curve and re-scaled the horizontal axis (time axis) to the unit interval $[0,1]$. Additionally, we applied linear interpolation to the force values, aligning them to an evenly spaced grid. That time re-scaling ignores duration of steps and the variation of speed across people, which instead were retained as walking speed and distance clinical variables. The top right panel of Figure 1 presents the collection of vGRF curves shown in the first panel, following this processing. Those curves are also color-coded according to their respective walking speeds. Similar results were achieved using the same processing steps for the apGRF and mlGRF curves, and are shown in the bottom left and bottom right panels of Figure 1, respectively.

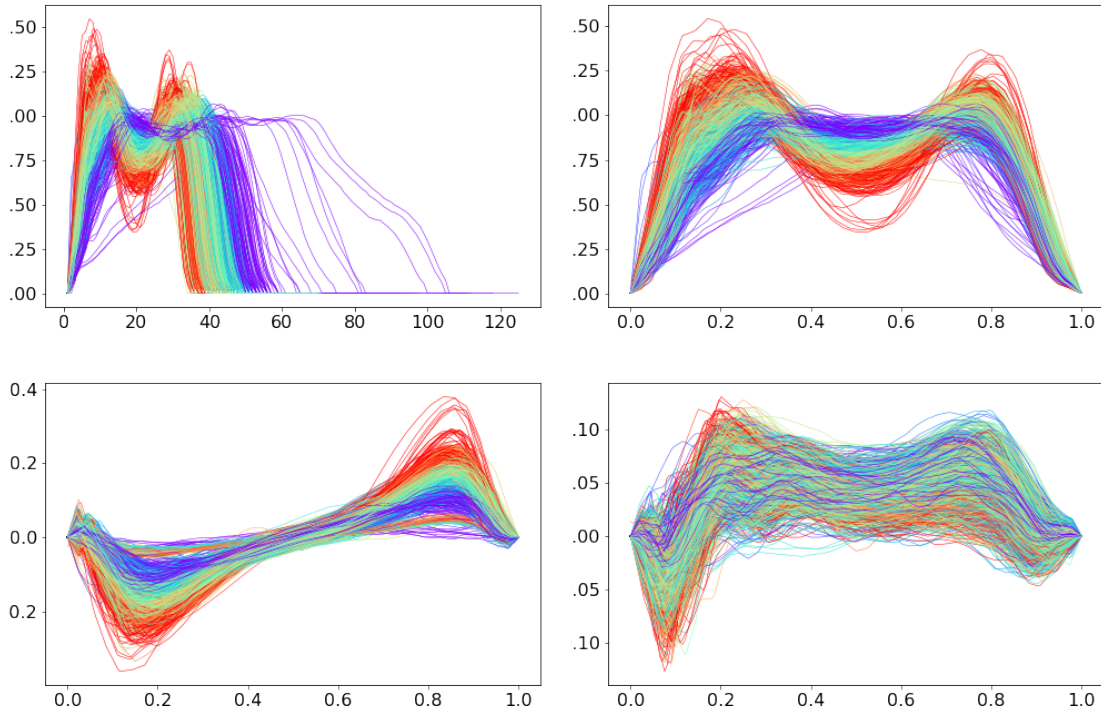


Figure 1: Top left panel: Raw vertical ground reaction force (vGRF) curves before processing, colored by walking speed. Top right: The same curves after re-scaling and interpolation of the time axis . The common rainbow color palette descends from fastest walking speed (red) to slowest (purple). Bottom row panels show apGRF curves (left) and mlGRF curves (right) after the same processing of the time axis. Note that the vertical axis (measured in N/kg, i.e. percentage of body weight) of each panel is scaled to the data it displays.

2.1 Conventional discrete summaries

Most relevant studies of GRF data, such as those in [Messier et al. \(1992\)](#), [Hunt et al. \(2006\)](#), [Zeni Jr and Higginson \(2009\)](#), and [Wiik et al. \(2017\)](#), focus on discrete summaries (also called landmarks) rather than analyzing the full curves. These discrete summaries typically correspond to critical subphases of stance phase during gait, such as the first and second vGRF peaks (heel-strike and toe-off) and positive and negative peaks of the apGRF curve (braking and propulsion). In contrast, mlGRF curves are highly variable and therefore

more challenging to interpret and summarize (Costello et al., 2021). Consequently, GRF studies primarily analyze the vGRF and apGRF directions.

Traditionally, greater attention has been given to the first vGRF peak, as heel-strike is a primary indicator of compressive joint loads and has been consistently linked to knee OA onset and progression. However, recent work by Buck et al. (2024) (and references therein) indicated that the valley (reflecting mid-stance) and the second peak of the vGRF curve are better predictors of knee OA-related symptoms. However, in order to represent most previous biomechanical studies related to knee OA, we focussed on the first vGRF peak and the braking and propulsion peaks of the apGRF curve in this analysis.

The first vGRF peak is defined in the references aforementioned as the maximum value within the first 50% (0-50%, heel-strike to midstance) of the stance phase (0-50%) (0-0.5 on the horizontal axis in Figure 1). Similarly, the apGRF braking peak is defined as the minimum value over the first 50% of the stance phase, and the apGRF propulsion peak is defined as the maximum value over the second 50% (50 – 100%, mid-stance to toe-off) of the stance phase (0.5-1.0 on the horizontal axis in Figure 1).

3 Shape-based functional data analysis

3.1 Elastic shape analysis

The goal of our analysis was to characterize patterns of variation in gait using information in the full force curves. Many data sets of curve data have variation that appears to be either vertical or horizontal in nature. This variation is termed *amplitude* and *phase* variation, respectively. In this context, horizontal variation is viewed as a potentially important aspect of gait, while in other contexts variation it may represent temporal misalignment.

The curves shown in Figure 1 exhibit interesting variation of both types. In particular, there is clear phase variation in the timing of the vGRF and mlGRF peaks, as well as the shift from posterior to anterior force in the apGRF curves.

Elastic warping of the time axis can provide aligned curves that better capture amplitude variation, as studied in Section 2.1 of Marron and Dryden (2021). This is important because poor alignment of curves due to phase variation can impact statistical methodology, potentially obscuring important geometric structure. An elastic warp is described by a curve, which is usefully thought of as a stretching and compression of the horizontal axis. The functions are aligned by finding the *Karcher mean* Tucker et al. (2013) which produces aligned functions and warping functions and will be defined later on. A warping function: $\gamma(x) : [0, 1] \rightarrow [0, 1]$ is strictly increasing, invertible, and *diffeomorphic*, in other words the function and its inverse are smooth. The collection of such warp functions serve as *phase* data objects.

Aligning points across functions is often referred to as *registration*. Many conventional Functional Data Analysis (FDA) techniques rely on the \mathbb{L}^2 norm, which simplifies computations into point-wise evaluations. While point-wise computations involve *vertical registration*, other methods focus on the *shape* of functions. L^2 -based methods present well-known challenges, as detailed in Marron et al. (2015). *Elastic shape analysis*, proposed in Srivastava et al. (2011); Tucker et al. (2013), uses the warp-invariant Fisher-Rao metric to overcome the limitations of conventional \mathbb{L}^2 -based alignment techniques. This approach is the first to enable fully automatic (meaning that no manual tuning is needed) shape-based registration. For each curve, the elastic shape analysis method computes the warp needed to align its peaks to a template mean curve, called the Karcher mean. The Karcher mean template is equivalent to the mean curve of the collection of aligned curves.

The key idea of this method is to define an equivalence relation between curves. *Amplitude* (or called *shape* in [Srivastava et al. \(2011\)](#); [Wu et al. \(2024\)](#)) of the data objects are equivalence classes. Two curves $f_1(x)$ and $f_2(x)$ are called equivalent, $f_1 \sim f_2$, if there exists a warping function γ such that $f_1(\gamma(x)) = f_1 \circ \gamma(x) = f_2(x)$. Then, the set of all warps of a function f , given by

$$[f] = \{f \circ \gamma : \gamma \in \Gamma\},$$

is the amplitude equivalence class.

The Fisher-Rao metric defines a proper distance on the set of such equivalence classes. In the elastic shape analysis framework, a *Square Root Velocity Function* (SRVF) representation transforms the Fisher-Rao metric into the standard \mathbb{L}^2 metric, allowing for a natural framework for the computations required for curve alignment. The Karcher mean equivalence class is defined using this distance, along with the warping functions needed to align individual functions to the Karcher mean template. The SRVF of a function $f \in \mathcal{F}$ is given by $q(t) = \text{sign}(\dot{f}(t))\sqrt{|\dot{f}(t)|}$. For any time warping of f by $\gamma \in \Gamma$, the SRVF of the warped function is given by $(q \circ \gamma)\sqrt{\dot{\gamma}}$, which we will denote by $q \star \gamma$ for convenience. Then, the warping functions needed to align a collection of curves f_1, \dots, f_n with corresponding SRVF representations, q_1, \dots, q_n , to a template mean μ_n are computed by solving the optimization problem:

$$\gamma_i^* = \operatorname{argmin}_{\gamma \in \Gamma} \|\mu_n - q_i \star \gamma\|_2^2.$$

In our analysis, we found substantial benefits by penalizing the amount of elasticity in the alignment of the curve. This is achieved by modifying the optimization problem to include a penalty term on the roughness of γ as follows:

$$\gamma_i^* = \operatorname{argmin}_{\gamma \in \Gamma} \|\mu_n - q_i \star \gamma\|_2^2 + \lambda \mathcal{R}(\gamma).$$

The penalty $\mathcal{R}(\gamma)$, controlled by the constant $\lambda > 0$, places a restriction on γ . In our approach we place a restriction on the second derivative of γ , where $\mathcal{R}(\gamma) = \int_0^1 \ddot{\gamma}(s) ds$. This places a restriction on the smoothness in γ and has the effect of keeping γ closer to the identity warp $\gamma(t) = t$, thus regulating the level of elasticity in the alignment. The case $\lambda = 0$ is referred to as *fully elastic alignment*, while $\lambda = \infty$ is non-elastic. This approach is similar to the penalty in [Wu and Srivastava \(2014\)](#).

For an intuitive overview of the elastic shape analysis procedure and a more detailed derivation of the template mean, see Section 9.1.3 of [Marron and Dryden \(2021\)](#).

The presence of phase variation observed in the GRF data motivated the application of elastic shape analysis to these data, from which we obtained a decomposition into amplitude and phase data objects. One possible approach to registering the GRF curve data is to apply the elastic shape alignment to each GRF component (vGRF, apGRF, mlGRF) separately. An analysis of amplitude and phase using this component-wise registration in the IDEA study data is detailed in Section 4.4 of [Xiang \(2023\)](#). However, that approach is less meaningful kinetically, as each component represents one direction of the same measured force. Instead, we adopted a more intuitive approach by treating the three components as a single multidimensional curve and applying elastic shape alignment to obtain a common set of warping functions. This approach allows us to focus on the phase aspects shared by all three components. Note that the Fisher-Rao mathematics extend straightforwardly to handle the multi-dimensional functions used here ([Srivastava and Klassen, 2016](#)).

A subset of GRF curves exhibited atypical vGRF or apGRF components, which posed challenges to aligning these curves with the rest of the data. Those GRFs were atypical in the sense that the vertical component lacked the two-peak structure expected of normal gait and appeared closer to unimodal, and/or the anterior-posterior component was close to

zero and relatively flat. Examples of these atypical cases are highlighted in the upper row of Figure 2, with representative atypical cases colored by walking speed and other curves in gray. Each panel in this row corresponds to one component of the original (unaligned) GRF curves.

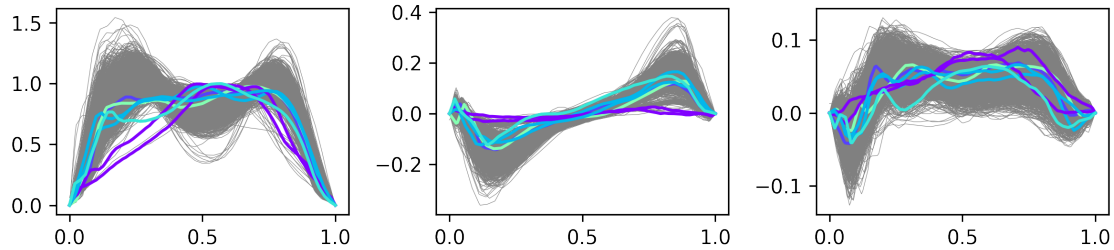


Figure 2: Left to right panels: vGRF, apGRF, and mlGRF curves. Examples of atypical GRF curves are highlighted, with representative atypical cases colored by walking speed and other curves in gray. These atypical curves lack the expected two-peak vertical structure or have near-zero, flat anterior-posterior components.

To address the lack of a common underlying structure, we registered the full dataset using the penalized elastic shape analysis procedure. By adjusting the elasticity parameter (λ), we aligned the full set of GRF curves without distorting the shape of the atypical curves. The upper and lower rows of Figure 3 display the alignment results for fully elastic ($\lambda = 0$) and our selected value of λ , respectively, with atypical cases colored by speed and other curves in gray as in Figure 2. The leftmost panels of Figure 3 show the warping functions for each λ value, while the aligned curves are in the second through fourth columns. Observe the sharp corners forming a staircase-like pattern in the warping functions for the fully elastic case. This pattern indicates over-alignment, requiring drastic stretching and compression to align curves with differing underlying structures, such as

unimodal curves. After testing several λ values, we selected $\lambda = 2$ to mitigate the staircasing effect observed when atypical curves are overaligned.

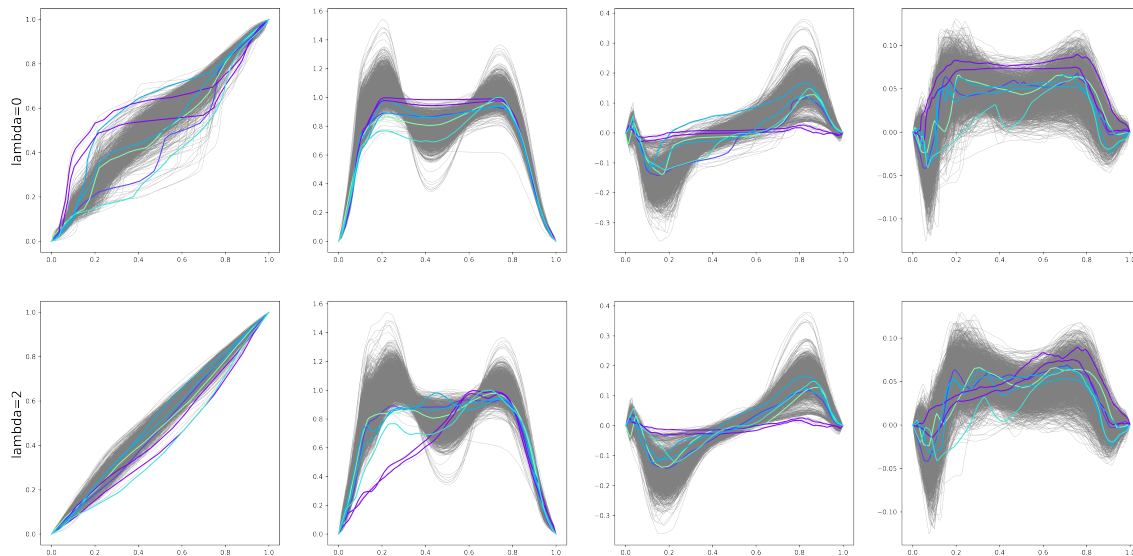


Figure 3: Alignment results using fully elastic ($\lambda = 0$) and the selected $\lambda = 2$ value, with atypical cases colored by speed and others in gray. The leftmost panels show the warping functions, and the aligned curves are in the second through fourth columns. The staircasing effect in the fully elastic case indicates over-alignment. The selected value $\lambda = 2$ mitigates this effect.

Next, we obtained amplitude objects by applying the (common) set of warping functions to each set of original GRF curves, which gives an intuitive representation of each component’s amplitude. The amplitude objects obtained for different values of λ are shown in the second through fourth columns of Figure 3.

3.2 Modes of variation

In the OODA terminology, a collection of members of the object space that summarize one component of variation and is in some sense one-dimensional is called a *mode of variation*.

For example, in the vector matrix case, a mode of variation is a rank-one matrix. We can obtain modes of variation through *Principal Component Analysis* (PCA), where each object is considered as a point in high dimensional space (column vector). For an introduction to PCA, see [Jolliffe \(2002\)](#). Performing PCA separately on the set of Fisher-Rao aligned curves for each GRF gives the amplitude modes ([Tucker et al., 2013](#)). The inputs to each PCA are the collections of curves in the second, third and fourth columns of the bottom row of [Figure 3](#).

[Figure 4](#) shows the modes of variation of the amplitude objects of the vGRF, where the curves are colored according to walking speed. The first mode of variation, shown in the first panel of the second row of that figure, is associated with walking speed and reflects the contrast in peak heights and valley depths. Faster walkers (indicated in red in the rainbow color scheme) generally exhibit higher peaks and lower valleys, while slower walkers (purple in the rainbow color scheme) have lower peaks and a shallower valley. The middle column of that figure displays the largest (dashed curve) and smallest (dotted curve) PC projections added back to the mean curve, which is shown as a solid black curve in each of the middle panels. The middle panel of the first mode shows that the slowest walkers (dotted curve) exhibit a vertical amplitude force that appears unimodal and does not exceed body weight (1 on the vertical axis), indicating that these walkers do not fully transfer their weight to the striking limb. This type of gait can be thought of as “shuffling.” The second and third modes of variation are about the second and first peak, respectively. The middle panel in the third row shows the largest and smallest PC2 projections added back to the mean curve, distinguished with a dashed (largest) and dotted (smallest) line type. These extremes show that variation in this mode is mostly in the height of the second peak. In the panel below, the extremes of the third mode indicate phase variation in the first peak that is unique

to the vertical component. The fourth mode of variation reflects the overall magnitude, particularly in the mid-stance phase. The second, third, and fourth PC projection extreme curves all suggest that some curves have a small third bump before the first peak. In gait analysis, this pattern is known as the *heelstrike transient* (HST), a rapid and transient rise in the vGRF immediately after ground contact. As discussed in [Blackburn et al. \(2016\)](#) and references therein, the presence and characterization (e.g. magnitude) of HST indicate impulsive loading, which influences cartilage degradation and symptoms of OA. However, [Blackburn et al. \(2016\)](#) also noted that methods for identifying HST can be unreliable. The amplitude modes of variation we identified offer a potentially viable method for reliably identifying and understanding the HST.

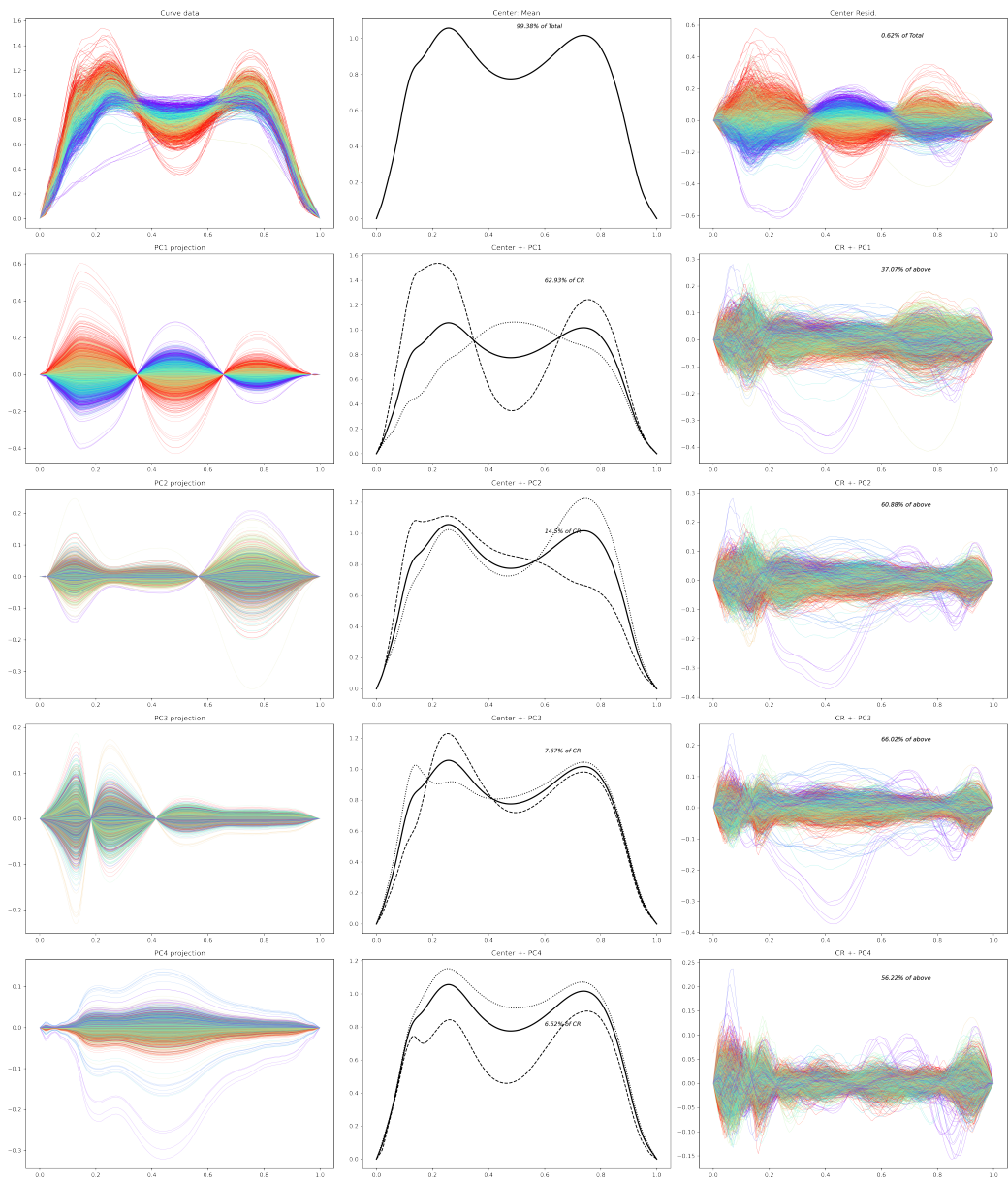


Figure 4: Modes of variation of the vGRF amplitude objects, shown in the top left panel. The first mode of amplitude variation, showing magnitude of the peaks and valley, is displayed in the second row, first panel. The panels in the middle column show the largest and smallest PC projections added back to the mean curve, while the solid black curve corresponds to the mean curve. The second and third modes of amplitude variation (third and fourth row, respectively) explain variation within each peak. The fourth mode indicates variation in overall magnitude, particularly of the valley, as seen in the middle panel of the last row.

Similar plots of the amplitude modes of variation of the components of apGRF and mlGRF are provided in Section 1 in the supplementary material.

Extracting phase modes of variation requires more careful consideration. Recall from Section 3.1 that the warping functions all have corresponding SRVFs that lie on the surface of a high-dimensional sphere in the function space. Thus, using PCA to identify phase modes of variation is essentially an approximation in the tangent space centered on the Karcher mean. In the case of warping functions, these SRVFs must also lie on the positive orthant Wu et al. (2024). It is demonstrated in Yu et al. (2017) that in cases of high variation, this tangent plane PCA may yield a distorted analysis, resulting in modes of variation that leave the positive orthant and consequently produce invalid warping functions. This phenomenon was also observed in our dataset. In such scenarios, a better decomposition of the variation can be achieved using the functional PCA methodology proposed by Yu et al. (2017), which is based on an improved PCA analogue for spheres known as Principal Nested Spheres (PNS) proposed by Jung et al. (2012). The PNS decomposition sequentially provides the best k -dimensional approximation U^k of the data for all $k = d - 1, d - 2, \dots, 0$ such that

$$S^d \supset U_{d-1} \supset \dots \supset U_1 \supset U_0.$$

For each k , the sphere U^k , called the k -dimensional *principal nested sphere*, is a submanifold of the higher dimensional principal nested spheres. The algorithm to find sample principal nested spheres is determined by iteratively minimizing an objective function to find the best-fitting subsphere, projecting the data to the lower dimensional sphere, and mapping to the original space through a relevant transformation. The signed residuals, defined as the signed length of the minimal geodesic joining the (projected and transformed) data points to the subsphere, serve as analogs of principal component scores. Chapter 8 of Marron and

Dryden (2021) provides further review of PNS and other geodesic-based methods.

We applied the PNS-based functional PCA methodology to the set of (common) warping functions to obtain phase modes of variation. We found that the great sphere decomposition from PNS yielded the most interpretable phase modes of variation because of weak interpretability of small sphere variation. Figure 5 depicts an intuitively useful notion of phase variation represented by warpings of the Karcher mean of the vGRF curves. The warping functions used to create these visualizations were generated by taking the inverse of the phase PNS projections added to the 45-degree line (identity warp). In each panel of the figure, the curves are colored based on the PNS scores for the corresponding mode, with cyan indicating the lowest scores and magenta indicating the highest. It is important to note that the curves are plotted in the order of the corresponding score, as over-plotting is an issue. The first mode (first panel) focuses on the timing of the first peak (maximum heel-strike force) and valley. The second mode in the next panel appears to explain variability in the closeness of the peaks - the cyan curves are the curves with peaks closer together and the magenta curves have peaks farther apart. The third mode represents an overall phase shift (left vs. right) and seems to suggest that curves having a small third bump before the first peak correspond with an earlier timing (cyan curves), especially an earlier second peak. The fourth mode appears to highlight variability in the timing of the second peak, independent of the rest of the curve.

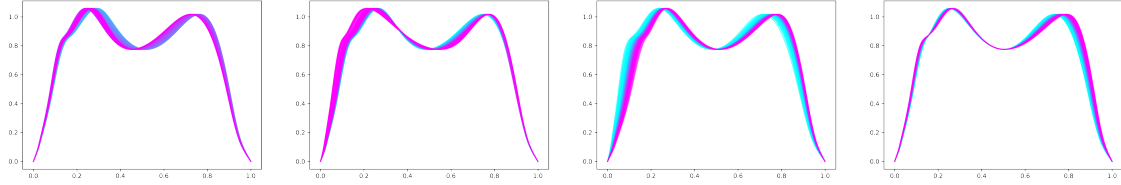


Figure 5: Visual representation of phase variation using warpings of the Karcher mean of the vGRF curves. Warping functions were generated by taking the inverse of the phase PNS projections added to the 45-degree line. Each panel shows curves colored by corresponding PNS scores, with cyan indicating the lowest scores and magenta indicating the highest. Curves are plotted in the order of the corresponding score to avoid over-plotting. The first panel (first mode) highlights timing variation of the first peak and valley. The second panel (second mode) shows variability in the closeness of the peaks. The third panel (third mode) represents an overall phase shift, suggesting earlier timing for curves with a small third bump before the first peak (cyan). The fourth panel (fourth mode) emphasizes variability in the timing of the second peak, independent of the rest of the curve.

4 Comparison to conventional discrete summaries

We investigated the added value of analyzing patterns across the entire movement curve, as opposed to conventional discrete summaries of GRF curves. To assess this, we compared the predictive performance of predictors derived from our shape-based analysis of the full movement curves with conventional discrete summaries in predicting disease progression. The progression or worsening of knee OA is a critical outcome in disease treatment studies. The standard method for evaluating *OA structural progression* involves measuring the joint space width (JSW) in millimeters on radiographic images, with a threshold set for the change in JSW to define progression (Ornetti et al., 2009). In the IDEA study, JSW was measured at baseline and at the 18-month follow-up visit. In this analysis, we used the change in JSW between baseline and 18-month follow-up as a dependent variable to

compare full-curve predictors with conventional discrete summary predictors.

Change in JSW measurements were missing for 129 out of the 454 IDEA participants. The missing values for JSW change are shown in the last column of the heatmap in Figure 4 in the supplementary material, with red lines indicating missing values. The rest of that figure is discussed in Section 4.2. The reasons for the missing values were not reported in the data, but a comparison of clinical data for participants with and without JSW measurements showed no apparent sampling bias. Following the criteria in Hunter et al. (2015) and Loeser et al. (2016), participants with a change in JSW of ≥ 2 mm were considered to have malpositioning between baseline and follow-up radiographs and were excluded from the analysis. This led to 6 exclusions, leaving a total of 319 participants with an appropriate change in the JSW data for our analysis.

To create predictors derived from our full-curve analysis, we combined scores for 16 distinct modes of amplitude variation from three types of curve data objects (vGRFs, apGRFs, and mlGRFs) and phase variation. Each mode is represented by either a set of amplitude PC scores or PNS phase scores. Below are listed the 16 sets of scores that together formed our predictor variables:

- PC1-PC4 scores of the vGRFs amplitude data objects (studied in Figure 4);
- PC1-PC4 scores of the apGRFs amplitude data objects (studied in Figure 1 in the supplementary material);
- PC1-PC4 scores of the mlGRFs amplitude data objects (studied in Figure 2 in the supplementary material);
- Great sphere PNS1-PNS4 scores of the common phase data object (studied in Figure 5).

We developed a set of predictors based on conventional discrete summaries of GRF curves found in the literature, including the first peak of the vGRF curve (maximum over 0 – 50% of the stance), the minimum value of the apGRF curve (minimum over 0 – 100% of the stance) and the maximum value of the apGRF curve (maximum over 0 – 100% of stance).

Using change in JSW as the dependent variable, we conducted a comparison of multiple linear regression models. We first used either our full-curve predictors or the set of conventional discrete summaries as independent variables. The coefficient of determination R^2 for the model with full-curve predictors was 0.027 and significantly different from zero, while the coefficient R^2 for the model with conventional discrete summary predictors was 0.002 and not significantly different from zero. Although both R^2 values were small, the model with full-curve predictors was a much stronger predictor of JSW change. Osteoarthritis (OA) is a multi-system condition influenced by various factors beyond the biomechanics studied here, including metabolic, inflammatory, post-injury, and aging-related changes. Given this complexity, it is unsurprising that the R^2 values are low.

Considering the complexity of OA disease and that the R^2 measure may arbitrarily favor larger models, a more nuanced comparison is appropriate to confirm the value added by using full-curve predictors. With this motivation, we conducted F-tests for nested models to provide a more robust comparison, detailed in the following section.

4.1 Nested model comparison

We assessed the value added of full-curve predictors over conventional discrete summaries by comparing nested linear regression models of the predictor sets. For predicting change in JSW, we computed the F-ratio of a full model containing both the full-curve predictors

and conventional discrete summaries versus a reduced model containing only the full-curve predictors. Similarly, we computed the F-ratio of the same full model against a reduced model containing only the conventional discrete summaries. This nested model comparison allowed us to assess the relative value of full-curve versus conventional discrete summaries by a formal hypothesis test. The null hypothesis of an F-test for nested model comparison states that all additional predictors in the full model have coefficient values of 0. Failing to reject the null hypothesis when the reduced model contains the full-curve predictors suggests that the conventional discrete summaries do not add predictive value beyond the full-curve predictors. Conversely, rejecting the null hypothesis when the reduced model contains the conventional discrete summaries indicates that the full-curve predictors offer additional predictive value not captured by conventional discrete summaries alone. Similar interpretations apply when reversing the roles of the full-curve and conventional discrete summaries.

The reduced model with only full-curve predictors was not rejected at the 0.05 significance level (p-value 0.3), whereas the reduced model with only conventional discrete summary predictors was rejected (p-value 1×10^{-5}). This comparison indicates that full-curve predictors offer greater predictive performance and explain more variation in the important disease indicator, the JSW change. However, predicting the change in JSW (or disease progression) is challenging. Therefore, in the following section, we further evaluate the value added by full-curve predictors over conventional discrete summaries by considering clinical traits collected in the IDEA study as outcome variables.

4.2 Predicting clinical traits

Various clinical traits relevant to patient health, OA severity, and pain/functionality were collected as part of the IDEA study. These included data from the participant level on sociodemographics, pain, mental and physical health, OA severity, and others. We used a subset of these clinical traits as dependent variables to compare full-curve predictors with conventional discrete summaries using the same nested model procedure as before. We selected 40 out of 72 clinical traits for analysis by excluding those that were redundant with other traits and those with a high number of missing values.

Figure 4 in the supplementary material shows a heat map of missing values after removing redundant traits, with blue lines indicating missing values for each clinical trait. The first 40 traits in that figure are the selected ones. Recall that the last column in that figure corresponds to change in JSW, analyzed separately in Sections 4 and 4.1. Note that more data are available for selected clinical traits, justifying a separate analysis of disease progression using the JSW change discussed in Sections 4 and 4.1. Since the selected traits had relatively few missing values, we imputed the remaining missing values using the mean value of each corresponding trait. Table 1 in the supplementary material provides an overview of the selected clinical data, including abbreviated trait names, brief descriptions, and trait types.

For each clinical trait, we repeated our comparison of multiple linear regression models, with the trait serving as the dependent variable. As before, we first used either our full-curve predictors or the set of conventional discrete summaries as independent variables. We maintained a consistent approach across all models without specifically addressing binary/ordinal variables or potential multicollinearity. While multiple linear regression may be more conservative in such scenarios, our primary aim was to give a fair comparison

of predictive performance under the same approach rather than maximizing predictive power.

Figure 6 presents a scatter plot, with each axis representing the value R^2 for the models that use the respective predictor set. The R^2 values were significantly different from zero for all models using full-curve predictors. In contrast, for models where fear of falling, smoking status and history of cancer were dependent variables, the R^2 values were not significantly different from zero when using conventional discrete summaries as predictors. These points are colored red in the figure, while green points indicate that the R^2 values are significantly different from zero for models based on conventional discrete summaries. Although movement curve predictors are not expected to be associated with smoking status and a history of cancer, they may be reasonably associated with fear of falling.

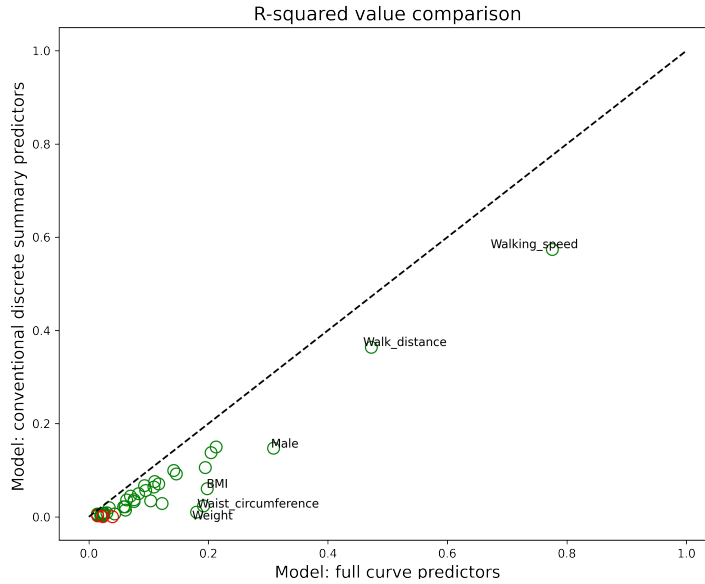


Figure 6: Scatter plot of R^2 coefficient of determination values for models using full-curve predictors versus conventional discrete summaries as predictors. Red points indicate dependent variables where R^2 values were not significantly different from zero for conventional discrete summaries. Green points indicate significant R^2 values for conventional discrete summary predictors. All points lie below the diagonal line ($x = y$), showing higher R^2 values for models based on full-curve predictors. Points farther from the diagonal represent greater differences in R^2 values. The farthest points correspond to walking speed, body weight, waist circumference, male gender, BMI, and walking distance, which are labeled in the figure.

All points lie below the diagonal line ($x = y$), shown as a black dashed line in the figure, indicating that R^2 values for models based on full-curve predictors are consistently higher than those for conventional discrete summary predictors. Points farther from the diagonal represent greater differences in R^2 values between the two predictor sets. The points farthest from the diagonal correspond to models with walking speed, body weight, waist circumference, male gender, BMI, and walking distance as the dependent variables, and these points are labeled in the figure.

Despite generally low R^2 values for both predictor sets, full-curve predictors consistently explain more variation in clinical traits, suggesting that they capture more information than

conventional discrete summaries.

4.3 Nested model comparison for predicting clinical traits

A nested model comparison again provided further insight into the added value of full-curve predictors. For predicting each clinical trait, we computed the F-ratio for a full model containing both full-curve and conventional discrete summary predictors versus reduced models with only full-curve predictors or only conventional discrete summaries.

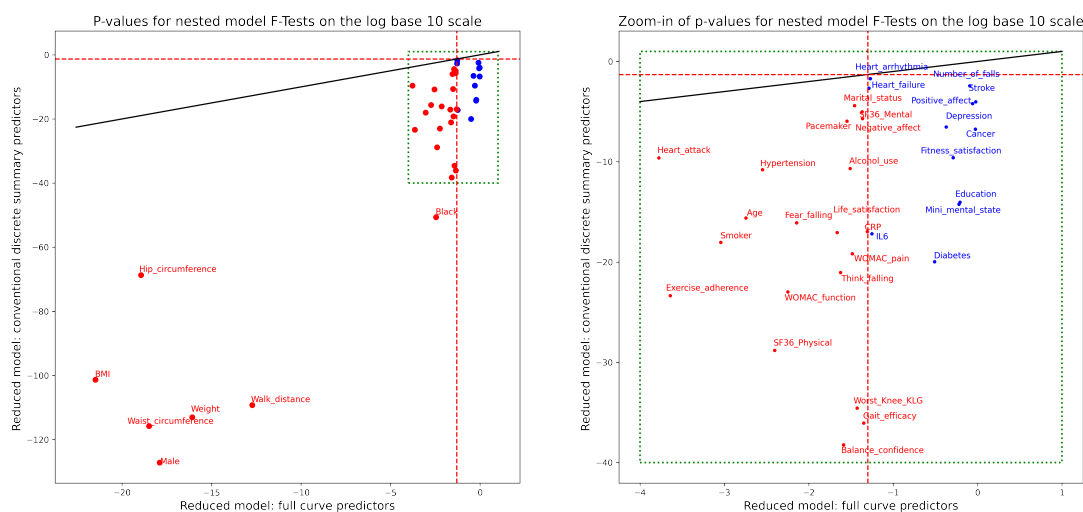


Figure 7: Left panel: Scatterplot of p-values from F-tests of nested models on a logarithmic scale (base 10). The horizontal axis shows p-values for reduced models with full-curve predictors, and the vertical axis shows p-values for reduced models with conventional discrete summary predictors. All points fall below the solid black line ($x = y$), indicating larger p-values for full-curve predictors. The red dashed line marks the $\log_{10}(0.05)$ significance threshold. Red points denote models where both reduced models were rejected at the 0.05 level, while blue points indicate models where only the reduced model with conventional discrete summary predictors was rejected. Labeled points show the most significant discrepancies, corresponding to the largest positive differences in R^2 values. Right panel: Zoomed-in view of the red and blue points in the upper right corner of the left panel, outlined by the dashed green box.

The left panel of Figure 7 displays a scatterplot of p-values resulting from F-tests of

nested models, shown on a logarithmic scale with base 10. The horizontal axis represents the p-values for testing reduced models with full-curve predictors, while the vertical axis represents those for testing reduced models with conventional discrete summary predictors. A solid black line indicates equal p-values for both reduced models (the line $x = y$). In particular, all points fall below this line, meaning that the p-values for reduced models with full-curve predictors are consistently higher than those for conventional discrete summary predictors.

A red dashed line marks the $\log_{10}(0.05)$ threshold on both axes, corresponding to the 0.05 significance level. The red points represent models where both reduced models were rejected at this significance level. The discrepancy in scale between the axes suggests that our full-curve predictors add substantially more value to the models than conventional discrete summaries. The points with the most pronounced discrepancies are labeled by the dependent variable. These variables are consistent with our previous comparison of R^2 values, indicating the largest positive differences in R^2 values between models based on full-curve predictors and those based on conventional discrete summaries.

The blue points represent models where the reduced model with full-curve predictors was not rejected, while the reduced model with conventional discrete summary predictors was rejected, indicating no predictive value from the addition of conventional discrete summaries. In particular, no points appear above the horizontal red dashed line, which means that the reduced model with conventional discrete summary predictors was always rejected, indicating that full-curve predictors consistently add predictive value.

The right panel of Figure 7 provides a closer examination of the red and blue points in the upper right corner of the left panel, outlined by the dashed green box.

The variable walking speed is not shown in Figure 7 because the p-value for the reduced

model with conventional discrete summary predictors was essentially 0.0 (due to computational precision), which would result in negative infinity on the logarithmic scale. For the reduced model with full-curve predictors, the p-value was approximately 1.785×10^{-15} (roughly -14.785 on the logarithmic scale). These results indicate that both reduced models are rejected at the significance level 0.05, but full-curve predictors add significantly more value than conventional discrete summaries, similar to the red points labeled in Figure 7.

5 Conclusion

This paper quantitatively compares the information contained in the data objects of the complete GRF curve versus conventional discrete summaries on disease progression and clinical profiles of patients with OA, demonstrating the greater value of analyzing the full curves. We employ a straightforward nested model comparison to highlight this difference. Furthermore, our shape-based approach offers an intuitive representation of full movement curves, applicable in broader analyses, and reveals insightful modes of variation. Our work is among the first to demonstrate the superior predictive potential of full movement curves over conventional discrete summaries and to utilize these representations for predicting disease progression.

SUPPLEMENTARY MATERIAL

Supplement to Elastic Shape Analysis of Movement Data: Additional figures and tables, with accompanying brief discussions. (pdf)

Funding

The research reported in this paper was partially supported by NIAMS P30 AR072580 and K24 AR081368. The research of Jan Hannig and J. S. Marron was partially supported by NSF Grant DMS-2113404. The research of Ashley N. Buck was partially supported by NIAMS T32 AR082310. The IDEA study was supported in part by: National Institutes of Health—R01 AR052528-01 from the National Institute of Arthritis and Musculoskeletal and Skin Diseases, P30 AG21332 from the National Institute on Aging, M01-RR00211 from the National Center for Research Resources—and by General Nutrition Centers.

References

- Astephen, J. L., Deluzio, K. J., Caldwell, G. E. and Dunbar, M. J. (2008), ‘Biomechanical changes at the hip, knee, and ankle joints during gait are associated with knee osteoarthritis severity’, *Journal of orthopaedic research* **26**(3), 332–341. [2](#)
- Bjornsen, E., Berkoff, D., Blackburn, J. T., Davis-Wilson, H., Evans-Pickett, A., Franz, J. R., Harkey, M. S., Horton, W. Z., Lisee, C., Luc-Harkey, B. et al. (2024), ‘Sustained limb-level loading: A ground reaction force phenotype common to individuals at high risk for and those with knee osteoarthritis’, *Arthritis & Rheumatology* . [3](#)
- Blackburn, J. T., Pietrosimone, B. G., Harkey, M. S., Luc, B. A. and Pamukoff, D. N. (2016), ‘Comparison of three methods for identifying the heelstrike transient during walking gait’, *Medical Engineering & Physics* **38**(6), 581–585. [14](#)
- Buck, A. N., Lisee, C. M., Bjornsen, E. S., Schwartz, T. A., Spang, J. T., Franz, J. R., Blackburn, J. T. and Pietrosimone, B. G. (2024), ‘Biomechanical threshold values for

- identifying clinically significant knee-related symptoms six months following anterior cruciate ligament reconstruction’, *Journal of Athletic Training* . **2**, **7**
- Costello, K. E., Felson, D. T., Neogi, T., Segal, N. A., Lewis, C. E., Gross, K. D., Nevitt, M. C., Lewis, C. L. and Kumar, D. (2021), ‘Ground reaction force patterns in knees with and without radiographic osteoarthritis and pain: descriptive analyses of a large cohort (the multicenter osteoarthritis study)’, *Osteoarthritis and cartilage* **29**(8), 1138–1146. **3**, **7**
- Davis, H. C., Luc-Harkey, B. A., Seeley, M. K., Blackburn, J. T. and Pietrosimone, B. (2019), ‘Sagittal plane walking biomechanics in individuals with knee osteoarthritis after quadriceps strengthening’, *Osteoarthritis and cartilage* **27**(5), 771–780. **3**
- Dillon, C. F., Rasch, E. K., Gu, Q. and Hirsch, R. (2006), ‘Prevalence of knee osteoarthritis in the United States: arthritis data from the Third National Health and Nutrition Examination Survey 1991-94.’, *The Journal of rheumatology* **33**(11), 2271–2279. **2**
- Dryden, I. L. and Mardia, K. V. (2016), *Statistical shape analysis: with applications in R*, Vol. 995, John Wiley & Sons. **2**
- Felson, D. T. (2013), ‘Osteoarthritis as a disease of mechanics’, *Osteoarthritis and cartilage* **21**(1), 10–15. **2**
- Guilak, F. (2011), ‘Biomechanical factors in osteoarthritis’, *Best practice & research Clinical rheumatology* **25**(6), 815–823. **2**
- Hunt, M. A., Birmingham, T. B., Giffin, J. R. and Jenkyn, T. R. (2006), ‘Associations among knee adduction moment, frontal plane ground reaction force, and lever arm during

walking in patients with knee osteoarthritis’, *Journal of biomechanics* **39**(12), 2213–2220.

6

Hunter, D., Beavers, D., Eckstein, F., Guermazi, A., Loeser, R., Nicklas, B., Mihalko, S., Miller, G., Lyles, M., DeVita, P. et al. (2015), ‘The intensive diet and exercise for arthritis (idea) trial: 18-month radiographic and mri outcomes’, *Osteoarthritis and Cartilage* **23**(7), 1090–1098. 19

Jolliffe, I. T. (2002), *Principal component analysis*, Springer Series in Statistics, second edn, Springer-Verlag, New York. 13

Jordan, J. M., Helmick, C. G., Renner, J. B., Luta, G., Dragomir, A. D., Woodard, J., Fang, F., Schwartz, T. A., Abbate, L. M., Callahan, L. F. et al. (2007), ‘Prevalence of knee symptoms and radiographic and symptomatic knee osteoarthritis in African Americans and Caucasians: the Johnston County Osteoarthritis Project.’, *The Journal of rheumatology* **34**(1), 172–180. 2

Jung, S., Dryden, I. L. and Marron, J. S. (2012), ‘Analysis of principal nested spheres’, *Biometrika* **99**(3), 551–568.

URL: <https://doi.org/10.1093/biomet/ass022> 16

Lawrence, R. C., Felson, D. T., Helmick, C. G., Arnold, L. M., Choi, H., Deyo, R. A., Gabriel, S., Hirsch, R., Hochberg, M. C., Hunder, G. G. et al. (2008), ‘Estimates of the prevalence of arthritis and other rheumatic conditions in the United States: Part II’, *Arthritis & Rheumatism* **58**(1), 26–35. 2

Loeser, R., Pathmasiri, W., Sumner, S., McRitchie, S., Beavers, D., Saxena, P., Nicklas, B., Jordan, J., Guermazi, A., Hunter, D. et al. (2016), ‘Association of urinary metabolites

- with radiographic progression of knee osteoarthritis in overweight and obese adults: an exploratory study’, *Osteoarthritis and Cartilage* **24**(8), 1479–1486. [19](#)
- Marron, J. and Dryden, I. L. (2021), *Objected Oriented Data Analysis*, Chapman and Hall/CRC. [3](#), [8](#), [10](#), [16](#)
- Marron, J. S., Ramsay, J. O., Sangalli, L. M. and Srivastava, A. (2015), ‘Functional data analysis of amplitude and phase variation’, *Statistical Science* pp. 468–484. [8](#)
- Messier, S., Legault, C., Mihalko, S., Miller, G., Loeser, R., DeVita, P., Lyles, M., Eckstein, F., Hunter, D., Williamson, J. and Nicklas, B. (2009), ‘The intensive diet and exercise for arthritis (idea) trial: Design and rationale’, *BMC musculoskeletal disorders* **10**, 93. [1](#), [3](#)
- Messier, S., Mihalko, S., Legault, C., Miller, G., Nicklas, B., DeVita, P., Beavers, D., Hunter, D., Lyles, M., Eckstein, F., Williamson, J., Carr, J., Guermazi, A. and Loeser, R. (2013), ‘Effects of intensive diet and exercise on knee joint loads, inflammation, and clinical outcomes among overweight and obese adults with knee osteoarthritis the idea randomized clinical trial’, *JAMA : the journal of the American Medical Association* **310**, 1263–73. [1](#), [3](#)
- Messier, S. P., Loeser, R. F., Hoover, J. L., Semble, E. L. and Wise, C. M. (1992), ‘Osteoarthritis of the knee: effects on gait, strength, and flexibility’, *Archives of physical medicine and rehabilitation* **73**(1), 29–36. [6](#)
- Muniz, A. M. S., Manfio, E. F., Andrade, M. C. and Nadal, J. (2006), Principal component analysis of vertical ground reaction force: A powerful method to discriminate normal and abnormal gait and assess treatment, *in* ‘2006 International Conference of the IEEE Engineering in Medicine and Biology Society’, pp. 2683–2686. [3](#)

- Ornetti, P., Brandt, K., Heliö-Le Graverand, M.-P., Hochberg, M., Hunter, D., Kloppenburg, M., Lane, N., Maillefert, J.-F., Mazzuca, S., Spector, T. et al. (2009), ‘Oarsis-omeract definition of relevant radiological progression in hip/knee osteoarthritis’, *Osteoarthritis and cartilage* **17**(7), 856–863. [18](#)
- Sims, E. L., Carland, J. M., Keefe, F. J., Kraus, V. B., Guilak, F. and Schmitt, D. (2009), ‘Sex differences in biomechanics associated with knee osteoarthritis’, *Journal of women & aging* **21**(3), 159–170. [2](#)
- Srivastava, A. and Klassen, E. (2016), *Functional and Shape Data Analysis*, Springer. [10](#)
- Srivastava, A., Wu, W., Kurtek, S., Klassen, E. and Marron, J. S. (2011), ‘Registration of Functional Data Using Fisher-Rao Metric’, *arXiv preprint arXiv: 1103.3817*. [8](#), [9](#)
- Trentadue, T. P. and Schmitt, D. (2024), ‘Fourier analysis of the vertical ground reaction force during walking: Applications for quantifying differences in gait strategies’, *Journal of Applied Biomechanics* **1**(aop), 1–9. [3](#)
- Tucker, J. D., Wu, W. and Srivastava, A. (2013), ‘Generative models for functional data using phase and amplitude separation’, *Computational Statistics and Data Analysis* **61**, 50–66. [8](#), [13](#)
- Vos, T., Flaxman, A. D., Naghavi, M., Lozano, R., Michaud, C., Ezzati, M., Shibuya, K., Salomon, J. A., Abdalla, S., Aboyans, V. et al. (2012), ‘Years lived with disability (YLDs) for 1160 sequelae of 289 diseases and injuries 1990-2010: a systematic analysis for the Global Burden of Disease Study 2010’, *Lancet (London, England)* **380**(9859), 2163. [2](#)
- Wiik, A. V., Aqil, A., Brevadt, M., Jones, G. and Cobb, J. (2017), ‘Abnormal ground

- reaction forces lead to a general decline in gait speed in knee osteoarthritis patients’, *World journal of orthopedics* **8**(4), 322. **6**
- Wu, W. and Srivastava, A. (2014), ‘Analysis of spike train data: Alignment and comparisons using extended fisher-rao metric’, *Special Section, Electronic Journal of Statistics* . **10**
- Wu, Y., Huang, C. and Srivastava, A. (2024), ‘Shape-based functional data analysis’, *TEST* **33**(1), 1–47. **9, 16**
- Xiang, S. (2023), Binary Expansion Testing and Gait Force Analysis, PhD thesis, University of North Carolina at Chapel Hill. **10**
- Yu, Q., Lu, X. and Marron, J. (2017), ‘Principal nested spheres for time-warped functional data analysis’, *Journal of Computational and Graphical Statistics* **26**(1), 144–151. **16**
- Zeni Jr, J. A. and Higginson, J. S. (2009), ‘Differences in gait parameters between healthy subjects and persons with moderate and severe knee osteoarthritis: a result of altered walking speed?’, *Clinical biomechanics* **24**(4), 372–378. **6**
- Zhang, Y. and Jordan, J. M. (2010), ‘Epidemiology of osteoarthritis’, *Clinics in geriatric medicine* **26**(3), 355–369. **2**